

# In Vivo Imaging of Mammalian Embryos By NIR-I Photoacoustic Tomography and NIR-II Optical Coherence Tomography Using Gold Nanostars as Multifunctional Contrast Agents

**Sheng Zhang**

Southern Medical University

**Zhenyang Liu**

Southern Medical University

**Linlin Mao**

Southern Medical University

**Jian Wu**

Southern Medical University

**Di Zhang**

Southern Medical University

**Ruiyuan Liu**

Southern Medical University

**Li Qi (✉ [qili@smu.edu.cn](mailto:qili@smu.edu.cn))**

Southern Medical University

---

## Research Article

**Keywords:** Photoacoustic imaging, NIR II optical coherence tomography, gold nanostars, embryo

**Posted Date:** December 9th, 2021

**DOI:** <https://doi.org/10.21203/rs.3.rs-1094935/v1>

**License:**  This work is licensed under a Creative Commons Attribution 4.0 International License.

[Read Full License](#)

---

***In vivo* imaging of mammalian embryos by NIR-I photoacoustic tomography and NIR-II optical coherence tomography using gold nanostars as multifunctional contrast agents**

*Sheng Zhang*<sup>1</sup>, *Zhenyang Liu*<sup>2,3,4</sup>, *Linlin Mao*<sup>1</sup>, *Jian Wu*<sup>2,3,4</sup>, *Di Zhang*<sup>2</sup>, *Ruiyuan Liu*<sup>2\*</sup>,  
*and Li Qi*<sup>2,3,4\*</sup>

\*Correspondence: [ruiyliu@smu.edu.cn](mailto:ruiyliu@smu.edu.cn); [qili@smu.edu.cn](mailto:qili@smu.edu.cn)

## **ABSTRACT**

### **Background**

High resolution, strong contrast and multimodality visualization of live mammalian embryo is an important requirement for studying foetal development. Photoacoustic Tomography (PAT) and Optical Coherence Tomography (OCT) are two advanced imaging modalities that has been utilized for embryonic imaging. However, high contrast, multiscale and deep tissue visualization of live embryos remains challenging.

### **Results**

Here, we demonstrate the use of gold nanostars (GNS) as multimodality contrast agents for the visualization and differentiation of embryos *in vivo* using NIR-I PAT and NIR-II OCT. We perform NIR-I PAT imaging to confirm *in vivo* GNS accumulation in the foetuses, and then use a customized NIR-II OCT system to further reveal deep, contrast-enhanced micro features of freshly harvested embryos. We investigate two different GNS administration pathways, i.e. intravenous and intravaginal injection, and significant enhancement of signal, image contrast, and imaging depth are achieved for both PAT and OCT.

### **Conclusions**

These findings prove that PAT-OCT bi-modal imaging with GNS enhancement provides more accurate structural characteristic of live mammalian embryos, and thus reveal its potential for embryonic development visualization and early abnormality examination.

### **Keywords**

Photoacoustic imaging, NIR II optical coherence tomography, gold nanostars, embryo

## **Introduction**

The ability to obtain the structural and functional information of live mammalian embryos is an important requirement for investigating human anatomical and physiological development [1, 2]. Preclinical research on mouse embryo development during early organogenesis helps to understand human congenital defects [3, 4]. Conventionally, microscopic examination with histological sectioning provided the structural information of embryonic tissues, but failed to offer the functional knowledge during development [5]. Therefore, the exploration of non-invasive imaging techniques that can visualize live embryonic organs is greatly desired. To date, promising modalities for embryo imaging have been developed, including micro computed tomography (micro CT) [6], magnetic resonance imaging (MRI) [7], laser scanning confocal microscopy (LSCM) [8], ultrasound [9], multiphoton microscopy (MPM) [1] and so on. However, each technique has its inadequacy such as limited imaging depth, radiation damage, and complicated sample preparation procedures [10, 11]. Therefore, exploiting high-contrast, deep penetration and real-time dynamic imaging techniques for live mammalian embryos has been an urgent need.

Optical coherence tomography (OCT), as a non-invasive imaging method, has attracted enormous attention due to its high spatial resolution and three-dimensional imaging capability [12, 13]. Clinically, it has been used extensively in ophthalmic imaging [14], cardiovascular screening [15], brain examination [16] and so on. In developmental researches, OCT has been utilized for both structural and functional imaging of mammalian embryos with cross-sectional imaging capability at micrometre scale spatial resolution [17]. Real-time visualization of internal organs such as the beating heart has been demonstrated on freshly harvested early mouse embryo system [18, 19].

In addition, OCT is also a label-free imaging technology because the OCT signal comes from tissue optical backscattering. However, this also limits its sensitivity (suffered from noise) and specificity (lacking image contrast) [20]. During the recent years, contrast agents for OCT have been developed to tackle this problem and extend

its application to physiological, cellular, and molecular imaging. As one of the most promising OCT contrast agent, gold nanoparticles (GNP) with high refractive index sensitivity and strong scattering at the near infrared (NIR) window have attracted considerable research attention [21]. A series of gold nanoparticles have been studied, including gold nanorods [22], gold nanoprisms [23], gold triangular [24], and gold nanodisks [25]. Owing to the low tissue scattering and deep tissue penetration [26, 27], gold nanostars (GNS) emerged as a new kind of promising material for NIR imaging thanks to its high refractive index sensitivity and strong scattering at the second NIR (NIR-II, 1100~1400 nm) window [28]. GNS has been used in OCT imaging for contrast enhancement [29], however, its application in live embryo imaging has not been evaluated.

Moreover, gold nanoparticles exhibited highly efficient absorption in the NIR region, making it also suitable for photoacoustic tomography (PAT) imaging [30-32]. PAT has emerged as a non-invasive technology for 3D imaging of biological tissue with optical contrast and ultrasonic imaging depth [33-35]. In PAT, a short laser pulse illuminates the tissue, and the light absorbed results in temperature rise, causing the emission of ultrasound due to thermoelastic expansion. An array transducer outside the tissue boundary detects the ultrasound, from which the absorption energy distribution within the biological tissue is retrieved with the help of image reconstruction algorithms. Aided with exogenous agents such as GNPs, PAT has been shown to achieve tumor diagnosis [36], pharmacokinetic evaluation [37], and metabolism monitoring [38] and etc. Although imaging of mammalian embryos using PAT has been reported recently [39] however, GNPs have not been attempted in live embryonic PAT imaging.

Except for the feasibility of sharing the same contrast agent, for embryonic imaging, OCT and PAT are also complementary in terms of spatial resolution (OCT at ~10  $\mu\text{m}$  and PAT at ~100  $\mu\text{m}$ ), contrast mechanism (light scattering for OCT and light absorption for PAT), and imaging depth (OCT at ~2 mm and PAT at >20 mm). Therefore, with novel GNPs such as GNS, bimodal OCT-PAT is expected to achieve multi-contrast, multi-scale, and dynamic imaging of living embryos, and holds great

promise for future researches.

Therefore, in this contribution, we have displayed that GNS are promising OCT/PAT dual modal contrast agents for visualizing the histological structures of live embryos. For PAT imaging, we utilized a commercial cross-sectional PAT system with NIR-I band excitation. With the highly efficient absorption in the NIR region of GNS, high-contrast PAT images of embryos in living mouse was obtained and hour-long metabolism of the GNS was visualized. For OCT imaging, unlike most of the conventional systems which also use NIR-I band (e.g. ~800 nm) light source [40], we adopted a custom-built system with a NIR-II band swept-source laser (centre wavelength at ~1310 nm). With this system, the penetration capability and scanning speed were largely improved, and the NIR-II characteristic of GNS was successfully coped with. Owing to their surface plasmon resonance and high dissipation coefficient in the NIR II window, we found that GNS drastically augmented the dynamic scattering in tissues and significantly enhanced the sensitivity of OCT signal. Based on this, we reconstructed 3D images of E10.5 mouse embryos with immature organs clearly highlighted. Additionally, to demonstrate the capability of this GNS-enhanced PAT-OCT dual-modal imaging solution, we investigated the effect of two different agent delivery pathways, namely, intravenous and intravaginal pathways, and confirmed the contrast-enhanced performance and their corresponding metabolism characteristic of the agent *in vivo*. Our work proves that GNS-enhanced OCT-PAT bi-modal imaging provides more accurate structural characteristic of live mammalian embryos, and thus reveals its significant potential for not only the visualization of development process, but also the early examination of embryonic morphological abnormalities.

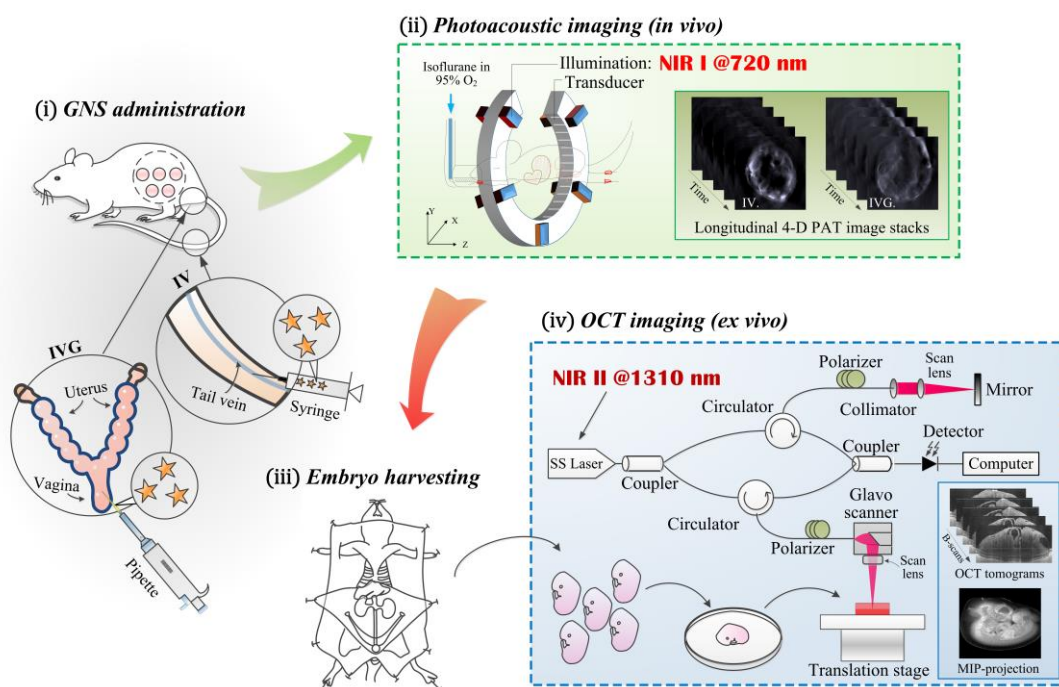


**Fig. 1** Schematic illustration of gold nanostar mediated NIR-II optical coherence tomography imaging and NIR-I photoacoustic tomography of live mammalian embryos.

## Materials and Methods

### Materials

All reagents and solvents were commercially available and utilized directly without further purification unless specified. Trisodium citrate, ascorbic acid, and HAuCl<sub>4</sub> was ordered from Alading LTD. UV absorption spectrum was performed with Thermofisher Evolution 300 spectropolarimeter. The size distribution was characterized by Zetasizer Nanoseries (Nano ZS90, Malvern Instrument Ltd.). The surface morphology was characterized by transmission electron microscopy.

### Synthesis, characterization, and functionalization of GNS

GNS were synthesized via a seed-mediated growth method. Gold seeds were prepared by addition of 1.5 mL trisodium citrate aqueous solution (1%) to 10 mL of boiling HAuCl<sub>4</sub> water solution (1 mM) under vigorous stirring for 15 min. 100  $\mu$ L of Gold seed was injected into 10 mL of HAuCl<sub>4</sub> solution (0.25 mM) under vigorous stirring, then 50  $\mu$ L of ascorbic acid (0.1 M) and 40  $\mu$ L of AgNO<sub>3</sub> (0.01 M) was simultaneously added. The product was purified by 3 cycles of centrifugation (8000

rpm, 10 min)/redispersion in water to provide the purified GNS.

### **OCT system**

All images were acquired using a customized swept source OCT system developed in our lab. The schematic of the system is shown (Scheme 1iv). The swept-source light source (AXP50125, Axsun, Canada) has a scanning rate of 100 kHz and a centre wavelength of 1310 nm with a full bandwidth of 110 nm, which provides an axial resolution of 3.67  $\mu\text{m}$  in water. The system employs a Michaelson interferometer implemented using optical fibres. The laser was first split into two arms, the reference arm and the sample arm. In the sample arm, the light beam was scanned by using a 2-axis galvo scanner and an objective lens (LSM03, ThorLabs, Newton, NJ), which provides a lateral resolution of 13  $\mu\text{m}$ . The reference arm used the same optical components as the sample arm (except for the galvo scanner) to compensate for dispersion. Light coming from the reference arm and the sample arm interfered at the second coupler and the signal was detected by using a balanced photodetector. All image reconstruction and analysis were performed using the acquired raw data with lab-built software based on C++ platform.

### **PAT system**

The PAT images were acquired using a commercial PAT imaging system (MOST InVision128, iTheraMedical GmbH, Germany) with the illumination provided by an Optical Parametric Oscillator (OPO) laser tuneable from 680 nm to 980 nm. The laser has a pulse width  $<10$  ns, repetition rate of 10 Hz, and a peak pulse energy of 60 mJ at 760 nm. The sample was excited through a ten-arm fibre bundle, which provides homogeneous, 360-degree illumination of approximately 8 mm width over the surface of the sample. The detection system (Scheme 1ii) consists of a ring-shape array formed by 128 transducers, covering an angle of  $270^\circ$  with a radius of 40.5 mm for signal measurement. The transducer has a centre frequency of 5 Mhz and send/receive bandwidth is 60%. The maximum field-of-view of this system is about  $50 \times 50$  mm, which is sufficient for imaging pregnant mice. The focused transducer elements are

cylindrically shaped, resulting in a slice thickness of around 800  $\mu\text{m}$ . The positioning device allows the movement with a minimum step of 0.1 mm along z-axis.

### ***In vitro* phantom studies of GNS**

To evaluate the image enhancement by GNS on OCT imaging, we performed a comparative imaging on the GNS solution and on distilled water. We first placed 1 mL of the solution/water on a microscope slide by using a pipette, and then transferred the slide to the translational stage under the OCT objective for cross-sectional OCT imaging. The OCT amplitudes of GNS solution and distilled water were characterized by taking B-scan images of the samples. Next, in order to acquire the photoacoustic absorbance spectra of GNS, centrifugal tubes (0.5 mL) were filled with various concentrations of probes. The amplitudes of GNS were characterized by taking PAT images at different wavelengths (730 nm, 760 nm, 780 nm, 800 nm, 850 nm, 875 nm) in the same view. The mean amplitudes of each GNS concentration were determined by circling probes in a ROI at the corresponding position on the image after reconstruction.

### ***In vivo* PAT imaging**

The living female mouse was first anesthetized with 2% isoflurane in oxygen. The anesthetized mouse was then placed in the animal holder with a thin layer of ultrasound gel around the circumference of the desired imaging region; and then wrapped up using a plastic foil membrane, which helped separate the mouse from water during imaging. The anesthesia port was connected to the animal holder, as well as the scanner. The mouse was then administrated with GNS solution with either intravaginal or intravenous injections. Immediately after the injection, the whole animal holder was moved to the imaging chamber filled with 34 °C water. Before and after injection of GNS solution, the PA images of the embryos was monitored via the PAT system at a time interval of 20 minutes for 3 hours. The imaging wavelength was 720 nm and the speed of sound was set to 1536 m/s.

### ***In vitro* OCT imaging**

For each OCT imaging section, a selected embryo was carefully placed on a plastic

thin film and then transferred to a petri dish. The use of the plastic thin film is to avoid the strong reflection of the petri dish surface during OCT imaging. The petri dish is then placed on a 3-axis translational stage and imaged by using the OCT system. During imaging, the maximum field of view for individual B-scans was 9 mm, but 3D scans were limited to a 7.5 mm × 7.5 mm area because of the quantity of data and the size of the embryo. Each B-scan consisted of A-lines in steps of 6 to 15 μm (adjustable according to the size of the sample), thus with 500 A-lines covering a range of 3 to 7.5 mm area on the sample. Each 3D scan contained 500 B-scans on the mouse embryo targets. Each 3D scan takes approximately 4 min, with 10 B-scans were recorded at each lateral position.

### **Animal experiments**

All animal experiments were approved by the Southern Medical University Animal Care and Use Committee (Guangzhou, China). ICR mice were used to establish the pregnant mouse model.

Preparation of pregnant mouse model: House mice in Individually Ventilated Cages (IVCs) on a 14-10 light cycle (on at 06:00, off at 19:00). Inject female mice with 5.0 IU PMSG around noon on Day 1. Approximately 48 hr post-PMSG injection, inject female mice with 5.0 U hCG on Day 3 and breed with stud males overnight. The morning after mating, checking for vaginal plugs was designated as embryonic day 0.5 (E0.5). Pregnant females were treated at E10.5. Embryos were dissected from the uterus in M2 medium (Sigma-Aldrich, USA). The dissection was performed as described [41].

### **Animal embryo harvest and preparation**

After the mouse was imaged by PAT, we sacrifice the mouse and harvested embryos for OCT imaging. The operating procedure is as follows: (i) The E10.5 mouse was sacrificed after their necks were broken and placed on wax plates; (ii) After disinfection with 75% alcohol, the skin of the lower abdomen was cut with scissors and forceps. The skin at the incision was held by two elbow haemostatic forceps and pulled to both sides of the head and tail to peel. The abdominal cavity was opened

with ophthalmic forceps and ophthalmic curving scissors to expose the uterus; (iii) One side of the uterus was clamped with ophthalmic tweezers to separate the uterine membrane. The angle of the uterus and the cervix were cut with ophthalmic curved scissors to separate the entire uterus carefully, and then the uterus was placed on a sterile filter paper to remove blood stains; (iv) The uterus was transferred into a petri dish containing PBS in the ultra-clean table and washed several times; (v) The uterus was moved into another petri dish containing PBS, the uterus was opened along the uterine mesangium with ophthalmic curved scissors, fetal mice with fetal membranes were removed with two ophthalmic forceps; (vi) The mouse embryo trunk was moved to another petri dish containing PBS and washed twice with PBS until there was no visible blood color.

## **Results**

### **Fabrication and optical property of gold nanostar (GNS)**

The GNS was prepared via a seed-mediated growth method according to the earlier report [42]. The GNS's optical properties were characterized using UV-vis spectroscopy. Its absorption maximum locates around 760 nm (Fig. 2B), which is favorable for photoacoustic imaging. The size and morphology of GNS were recorded by dynamic light scattering (DLS) and transmission electron microscopy (TEM) (Fig. 2A). GNS exhibit star structure with average diameter of ~40 nm. After irradiation (808 nm, 100 mW/cm<sup>2</sup>, 10 min), absorption spectrum of GNS changed slightly, and there was not any evidence of size change, confirming that the GNS exhibited excellent photostability (Fig. S1 and S2). Moreover, after storage at room temperature for 45 days, no obvious shift of the DLS of GNS was observed (Fig. S3), indicating a long-term stability.

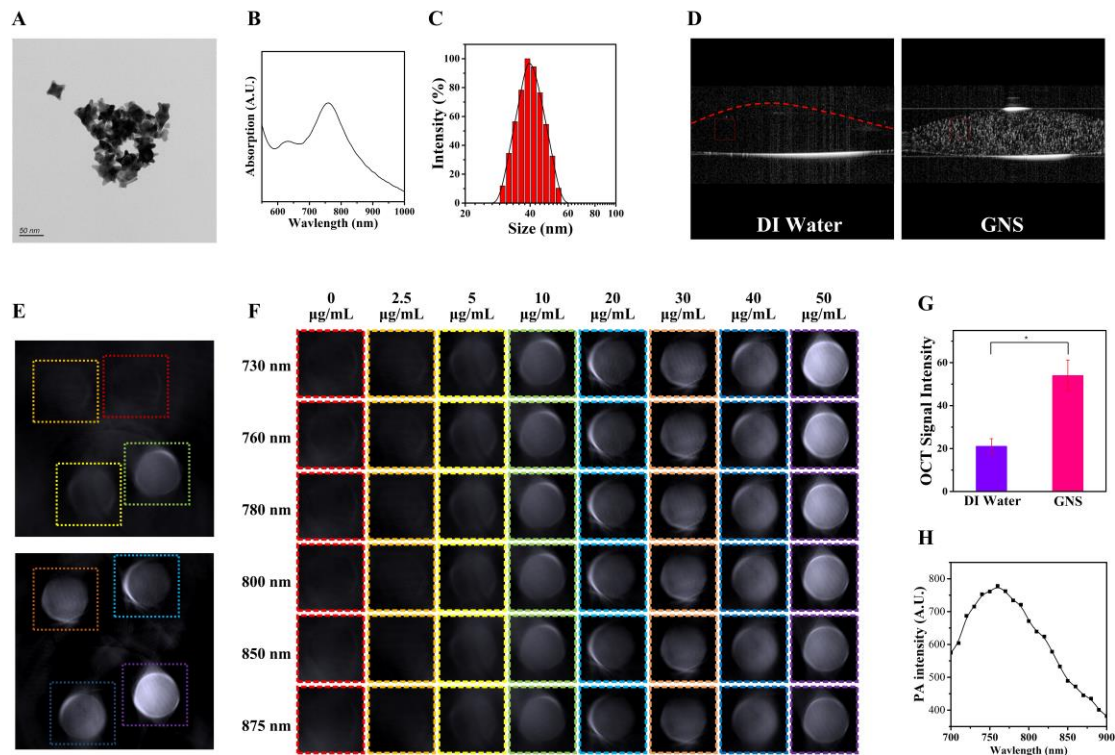


**Fig. 2** Property of GNS. **A** TEM of GNS. **B** The UV spectrum of GNS. **C** The Particle size distribution of GNS. **D** OCT imaging of DI water and GNS. **E** PAT images of GNS solutions with different concentrations. **F** Individual PAT images of the GNS solution at different wavelength and different concentrations. **G** OCT signal intensity of DI water and GNS. **H** Mean PA signal amplitude of 50 g/mL GNS solution.

### PAT property of GNS

To evaluate photoacoustic effect of GNS, a phantom study was carried out via a commercial photoacoustic tomography system. This PAT system has a wavelength tunable laser at the NIR-I window (tuning range 680-960 nm), and produces cross-sectional images at an in-plane resolution of 150  $\mu\text{m}$  (see Methods for the detail of the system). At each experiment, four 1 ml centrifuge tube were loaded with GNS solutions with different concentrations and imaged at the same time using the PAT system. The PAT imaging of the different phantoms is exhibited (Fig. 2E). The GNS demonstrate strong photoacoustic signal, and the signal intensity increases linearly with GNS concentration. We also got the images and measured PA signals of 50 g/mL GNS at different illumination wavelengths (Fig. 2F-H). The photoacoustic spectrum of the GNS exhibits maximal intensity around 760 nm, which agrees with the UV absorption profile.

## **OCT imaging of GNS**

Optical coherence tomography is a non-destructive imaging modality that provides tomographic images at micron-scale resolution with millimetre-scale field-of-view. In pre-clinical research applications (such as the recent work [40] also on GNP-enhanced embryonic imaging), current OCT imaging systems mostly employ NIR-I band light source (usually around 800 nm) and the spectral domain detection architecture. However, recent optical imaging literatures have shown that NIR-II band imaging outperformed NIR-I band imaging due to its superior tissue-penetration ability [43]. For OCT imaging in particular, it has also been demonstrated that a NIR-II band light source, together with a swept-source architecture, is able to achieve several folds' improvements on both imaging depth and image SNR compare to conventional OCT. In view of these, here we constructed a swept-source OCT system with a NIR-II band light source for the deeper and higher quality imaging of mouse embryos. The schematic of the system and the detail of the system is presented in the supplemental Methods. Our system provides 100 kHz A-line scan rate, 3.67  $\mu\text{m}$  depth resolution, and 13  $\mu\text{m}$  lateral resolution. Compared to the aforementioned conventional OCT systems [44, 45], this lab-built system provides higher SNR and faster imaging speed thanks to the swept-source and balanced detection architecture, and has much better penetration capability because of the NIR-II illumination wavelength (1260~1360 nm).

We first investigated the OCT property of GNS using the above system. The B-scan images of GNS solution at 50 g/ml and distilled water were acquired (Fig. 2D). Strong OCT signal from GNS was observed. The dispersed bright spots demonstrate the unique scattering characteristic of GNS. The mean OCT amplitude was investigated by monitoring the signal in the region of interest (400  $\mu\text{m}$ \* 50  $\mu\text{m}$ , red-solid box) at the top of each sample's B-scan. The GNS solution has nearly 2.6-times higher signal intensity than water. Notice that the actual signal enhancement should be larger because the GNS signal is scattered dispersedly within the measured region. All these results validated GNS could act as an optional mediator for OCT imaging.

### ***In vivo* PAT imaging of gold nanostar for embryo**

Encouraged by the excellent photoacoustic property of GNS, *in vivo* PAT imaging with E10.5 pregnant mice was carried out. To achieve the accumulation of the GNS in embryo, we administrated the GNS into pregnant mice via two different pathways: intravenous (IV) or intravaginal (IVG) injection. These two pathways result in two different GNS delivery mechanisms: for the intravaginal pathway, the delivered GNS should penetrate the embryonic membrane (decidua and Reichert's membrane) and then permeate into the embryo; for the intravenous pathway, the GNS will travel through circulation, and some of them reach the embryo through the placenta and the umbilical cord. Therefore, by this way, we can validate whether the GNS can be transported across the placental barrier, which protects the embryo during development and prevents damage of harmful substances from blood circulation [46], and accumulate in embryo to provide extra PAT contrast.

After administration, the PAT images of pregnant mice were recorded (Fig. 3). As can be seen, the embryos in pregnant mice after GNS administration via the two pathways both displayed photoacoustic signal, and high quality embryo structure was observed. Compared to the control embryos (0 min), overall image intensity was gradually increased after the injection of GNS, and the contour and details of individual embryos became much clearer. Moreover, the signal intensity was substantially increased after GNS administration, and maximum intensity of the embryo regions was reached at around 80 min for both IV and IVG injections. Interestingly, PAT imaging of mice via the IV pathway exhibited brighter signals around the edge of the embryos, whereas the IVG pathway images displayed signal enhancement in the whole embryo. This might be because of a stronger GNS permeation of the IVG pathway than the IV pathway. All these results confirmed that GNS could transport across the placenta and accumulate in the embryo.

Next, we performed PAT imaging of the harvested embryos to validate the permeation effect of the two pathways. PAT images of embryos with placenta and embryonic membrane, embryos with placenta, and embryos alone were acquired for the control, IVG and IV cases. In all cases (Fig. 3E-G), both the IVG and IV injected

embryos showed much higher signal intensity than the control embryos, and the IVG embryos achieved the highest intensity. This confirms that the IVG injection method provide the GNS with higher permeation to enter the embryo compared to IV injection. Nonetheless, all the above experimental results demonstrated the excellent contrast enhancement capability of the GNS in live embryonic PAT imaging regardless of the delivery pathways.

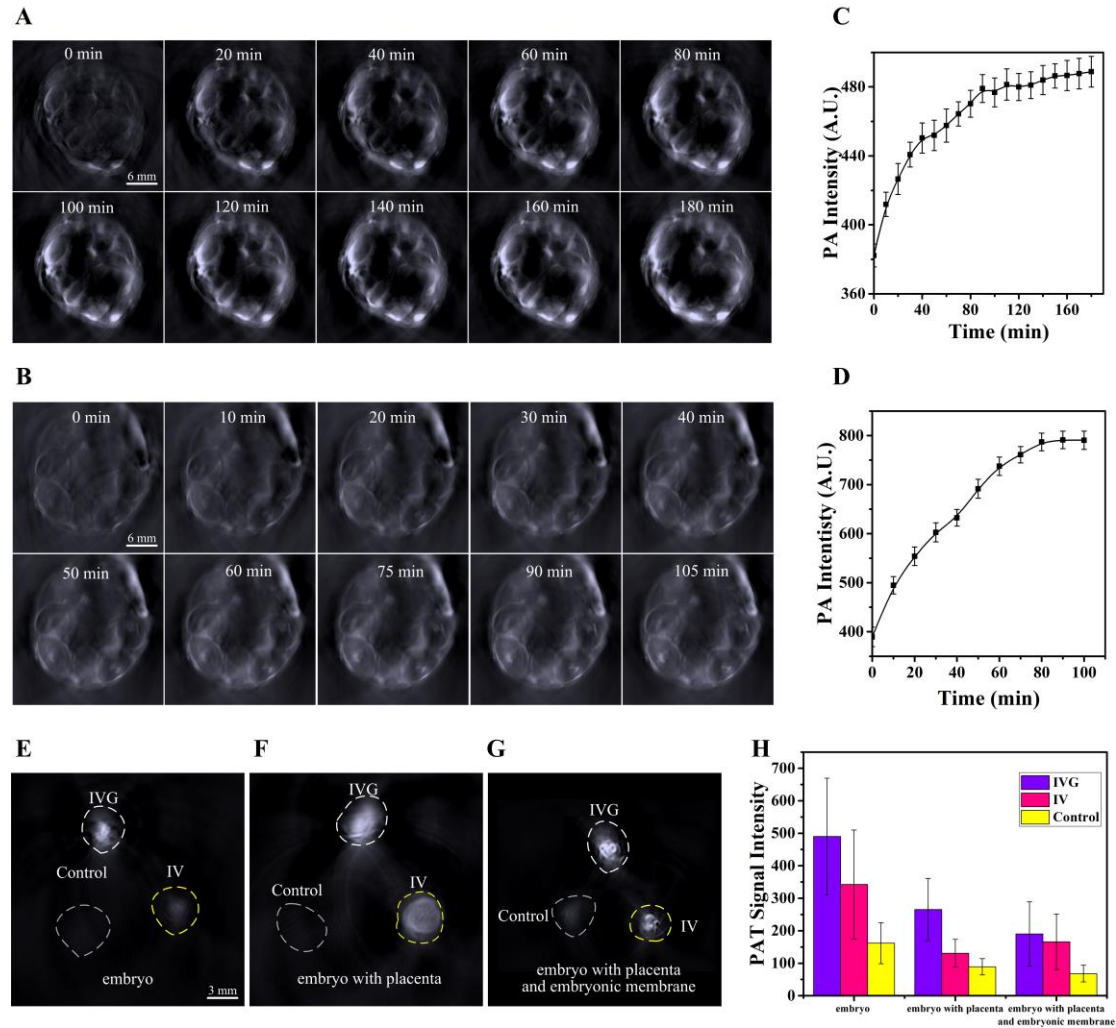


**Fig. 3** The PAT images of embryo. **A** *In vivo* PAT images of mouse embryos with intravenous injection of GNS. **B** Averaged PAT signal amplitude of the embryo region. **C** *In vivo* PAT images of mouse embryos with intravaginal injection of GNS. **D** Averaged PAT signal amplitude of the embryo region. **E** PAT images of the harvested embryo. **F** PAT images of the harvested embryo with placenta. **G** PAT images of the harvested embryo with placenta and embryonic membrane. **H** Signal intensity of E, F and G.

### Enhancement of contrast and depth of OCT images by GNS

We further carried out OCT imaging studies of freshly harvested E10.5 embryos.

After *in vivo* PAT imaging, the embryos were harvested and transferred to a petri dish and taken to perform 3-dimensional OCT imaging. Representative OCT B-scan images of the embryos under control, IVG and IV injections of GNS were exhibited (Fig. 4). Thanks to the NIR-II laser excitation, OCT imaging provided a greater penetration depth ( $>1$  mm), and visualized almost the entire harvested E10.5 embryos from top to bottom. Also can be seen, compared with the control group, the overall signal intensity of the OCT image has been improved after GNS administration. Next, we investigated the OCT signal intensity versus depth profiles to evaluate the effects of GNS treatment (Fig. 4B-D). As can be seen, both the maximum signal intensity and imaging depth were improved after GNS administration. For both the IV and IVG delivery pathways, similar signal enhancement was exhibited, and an averagely 40.12% increase of peak signal amplitude was achieved compared to the control cases.

Furthermore, the mean OCT signal intensity within the red solid-box regions (Fig. 4A) was quantified (Fig. 4F). Compared with the control group, the mean intensity of the GNS treated images significantly increased (+34% for IVG and +40% for IV).

To illustrate the enhancement on imaging depth by GNS administration, we produced OCT images at different depths by reslicing the 3D OCT image stack along the x-y sagittal plane, and the results are shown (Fig. 4E). Image contrast became much higher for both the IVG and IV images, especially in the depth regions from 412.776  $\mu\text{m}$  to 825.552  $\mu\text{m}$ . The edges and details of different structures (e.g. the heart, green arrow) (Fig. 4) were also clearer in OCT images with GNS injection. At greater depths (e.g. 825.552  $\mu\text{m}$ ), the OCT images of the control case had lost certain information around the centre of the embryo, whereas the OCT images of both IV and IVG GNS injection still conserved distinct structural details. Furthermore, we quantify the mean signal amplitudes within the red solid-boxes of different depths (Fig. 4E), and the result is displayed (Fig. 4G). Compared with the control group, the GNS treated samples provided significantly enhanced signal amplitude that agreed with the OCT B-scan results. Moreover, the signal increase for IV and IVG

administrations were similar, but as the imaging depth increased, the enhancement was dropped from 61.68% (at 412.776  $\mu\text{m}$ ) to 33.10% (at 825.552  $\mu\text{m}$ ).

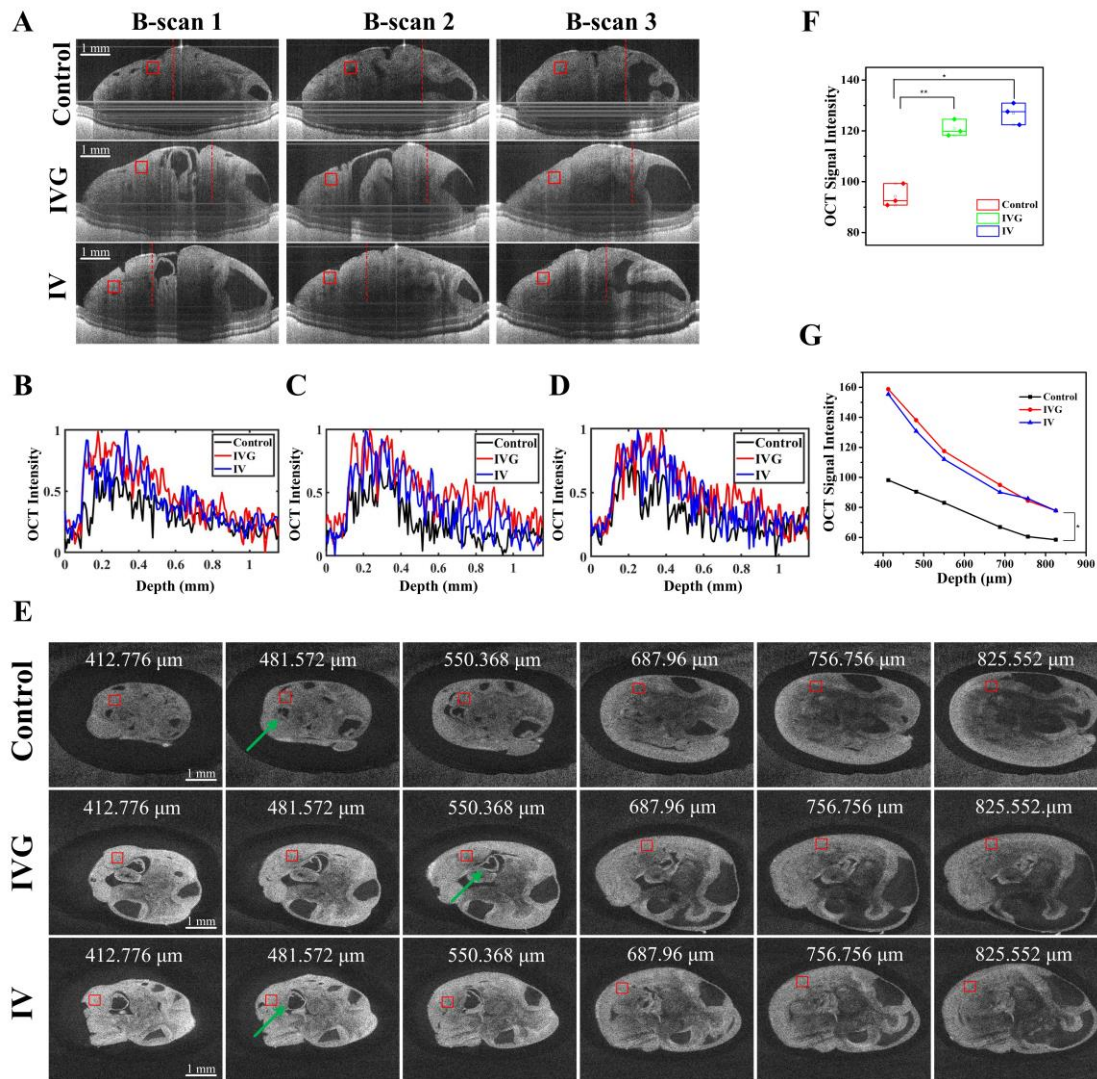


**Fig. 4** OCT imaging of embryos *in vitro*. **A** Representative OCT B-scan images of the harvested embryos. **B-D** OCT signal profile of the embryos corresponding to the red-dashed lines in B-scan 1 to 3 of a, respectively. **E** Mean OCT signal intensity within the red solid-box regions in B-scan 1 to 3 of a. **F** Lateral OCT images at different depths. **G** Averaged OCT signal intensity at different depths.

Next, the *en face* images of the embryos were generated via the maximum-intensity-projection (MIP) method to visualize the internal organs of the embryos (Fig. 5A-C). In all cases, major organs such as the spine, brain, heart and the optical vesicle were successfully visualized by OCT imaging, but in the embryos with GNS administration, the overall image contrast was better than the control embryo. As shown in the enlarged details of the blue and green dashed-boxes, the introduction

of GNS successfully enhanced the visibility of edges and cavities of the heart, and improved the resolution around the spine.

Finally, we performed 3D embryo reconstruction and visualization of the OCT images using the ImageJ software. The 3D reconstructed embryos at three different viewing angles were displayed (Fig. 5D-F). In the control case, the general structure of the embryo and the boundaries among the organs are difficult to identify, whereas in the IVG and IV cases, these image features were significantly improved. Specially, the IVG image shows a clear structure of the spine.

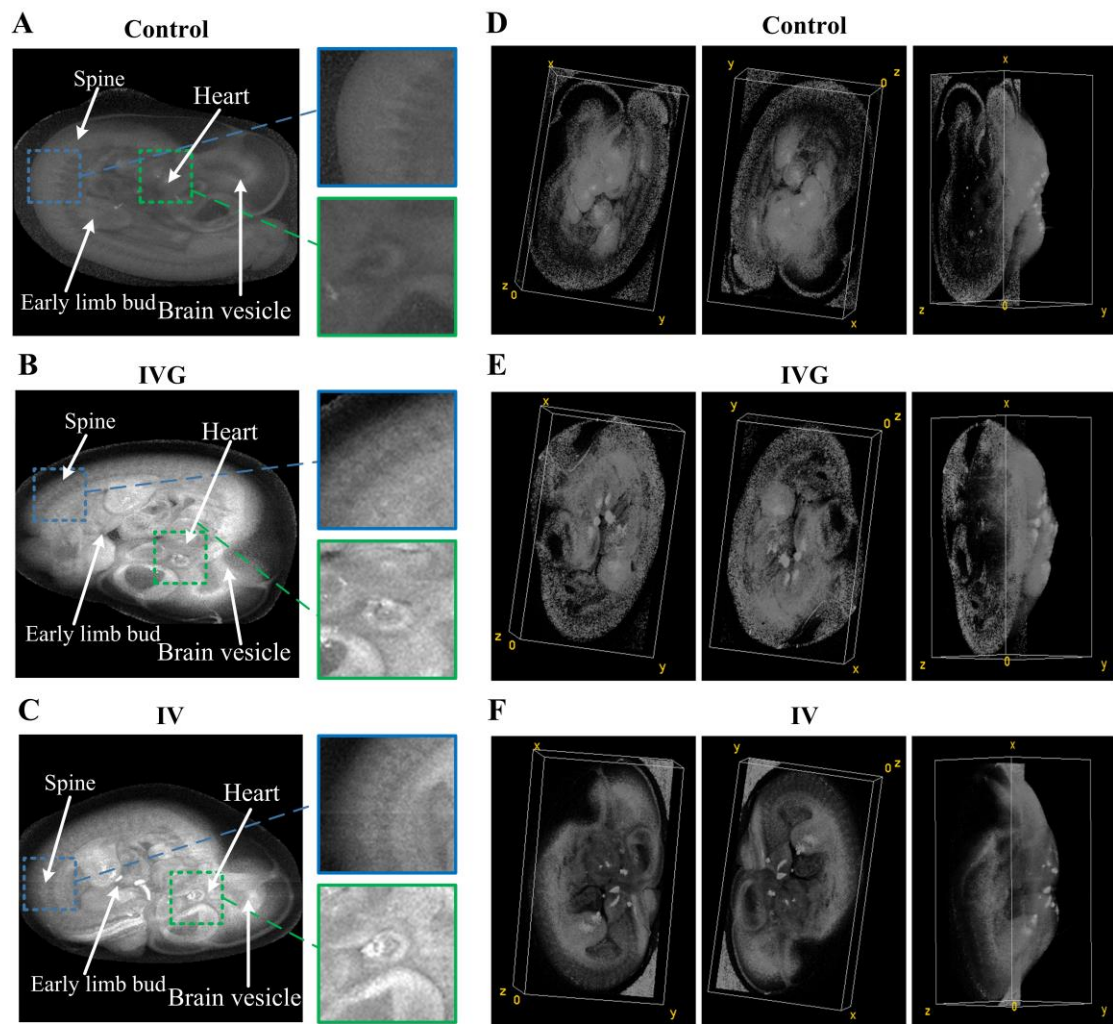


**Fig. 5** Maximum Intensity Projection (MIP) OCT images of the embryos. **A** Control. **B** Injection of IVG. **C** Injection of IV. 3D OCT embryo images at different viewing angles. **D** Control. **E** Injection of IVG. **F** Injection of IV.

## **Discussions**

In this work, we evaluated an innovative strategy to visualize the living embryo via Gold Nanostar mediated PAT and OCT. With our PAT and OCT excitations in NIR-I and NIR-II windows respectively, we demonstrated extra contrast provided by the GNS across a wide optical spectrum, and obtained multi-scale images of E10.5 embryos both *in vivo* and *in vitro*. GNS administration enabled significant contrast enhancement for both PAT and OCT: using PAT, multiple living embryos seated inside the mother's uterus intact were visualized in hour-long longitudinal imaging sections; using OCT, high-resolution and whole embryo 3-D visualization was achieved with better contrasting of internal organ borders. In addition, we further investigated the intravenous and intravaginal delivery pathways of GNS, and confirmed considerable signal enhancement for both OCT and PAT for either pathway. Our work proves that, together with GNS, PAT-OCT bi-modal imaging made possible the multi-contrast, multi-scale, and multi-NIR-spectrum visualization of living embryos, and thus holds great promise for various studies of morphological and functional changes during mammalian embryonic development.

## **Conclusions**

In conclusion, we provide an innovative strategy to visualize the living embryo *in vivo* via PA/NIR-II OCT dual modal imaging based on GNS. We demonstrated GNS could be delivered into embryos via intravenous injection or vaginal injection. GNS administration achieve embryos PA imaging *in vivo* and provide OCT imaging with accurate spatial orientation and better contrasting for the organs borders. Furthermore, GNS can present clearer 3D images of embryos. All these results confirmed that GNS can provide enhanced visualization of embryos using multimodal PA and NIR-II OCT to study the morphological changes during embryonic development *in vivo*.

## Supplementary Information

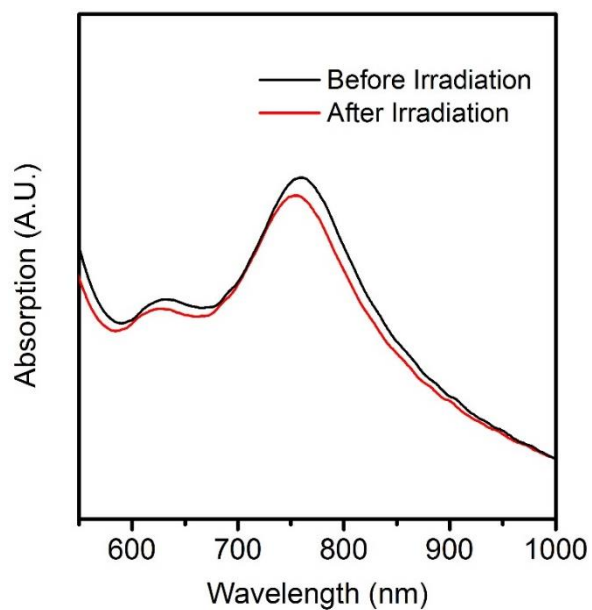


Fig. S1 The UV spectrum of GNS after 808 nm laser irradiation.

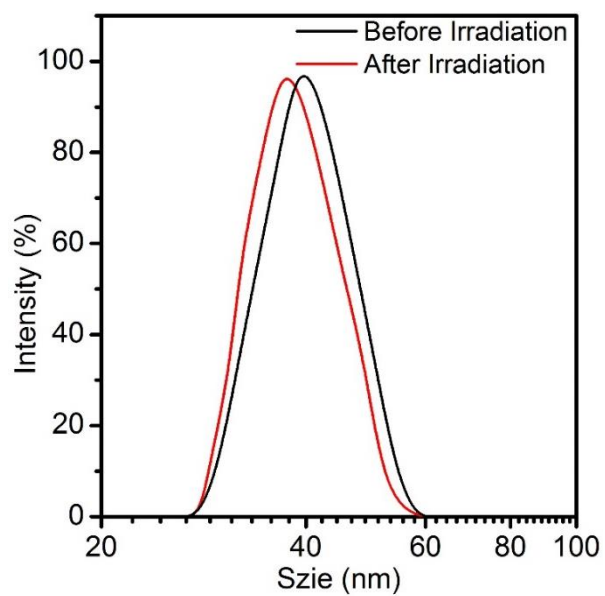


Fig. S2 The Particle size distribution of GNS after 808 nm laser irradiation.

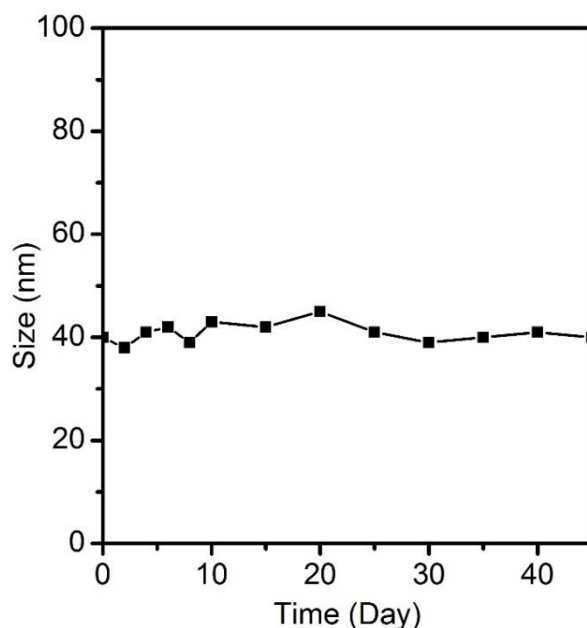


Fig. S3 The Particle size distribution of GNS stored at room temperature for a while.

### **Authors' contributions**

L. Q., R. L. and S. Z. conceived the project, designed the experimental schemes and supervised the research. S. Z., Z. L., and J. W. carried out the photoacoustic imaging experiments. S. Z., L. Q. and Z. L. carried out the optical coherence tomography experiments. R. L., D. Z. prepared the gold nanostar and performed characterization. S. Z. and L. M. contributed the animal preparation and embryo depilation. All authors participated in critical discussions of the results and writing of the paper.

### **Funding**

This work is supported by the Guangdong Basic and Applied Basic Research Foundation (2021A1515012542); Guangdong Pearl River Talented Young Scholar Program (2017GC010282).

### **Availability of data and materials**

All data generated or analyzed during this study are included in this published article.

### **Declarations**

### **Ethics approval and consent to participate**

Animal experiment is in accordance with the regulations of the Animal Ethical and Welfare Committee of Southern Medical University (SYXK2016-0167).

### **Consent for publication**

All authors agree to be published.

### **Competing interests**

The authors declare no conflict of interest.

### **Author details**

<sup>1</sup> Department of Cell Biology, School of Basic Medicine, Southern Medical University, Guangzhou, 510515, China. <sup>2</sup> School of Biomedical Engineering, Southern Medical University, Guangzhou, 510515, China. <sup>3</sup> Guangdong Provincial Key Laboratory of Medical Image Processing, Southern Medical University, Guangzhou, 510515, China. <sup>4</sup> Guangdong Province Engineering Laboratory for Medical Imaging and Diagnostic Technology, Southern Medical University, Guangzhou, 510515, China.

### **References**

1. Huang Q, Cohen MA, Alsina FC, Devlin G, Garrett A, McKey J, Havlik P, Rakhilin N, Wang E, Xiang K, et al: **Intravital imaging of mouse embryos.** *Science* 2020, **368**:181-186.
2. Nowotschin S, Hadjantonakis AK: **Live imaging mouse embryonic development: seeing is believing and revealing.** *Methods Mol Biol* 2014, **1092**:405-420.
3. Rossant J, Tam PPL: **Exploring early human embryo development.** *Science* 2018, **360**:1075-1076.
4. Moon AM: **Mouse models for investigating the developmental basis of human birth defects.** *Pediatr Res* 2006, **59**:749-755.
5. Norris FC, Wong MD, Greene ND, Scambler PJ, Weaver T, Weninger WJ, Mohun TJ, Henkelman RM, Lythgoe MF: **A coming of age: advanced imaging technologies for characterising the developing mouse.** *Trends Genet* 2013, **29**:700-711.
6. Ermakova O, Orsini T, Gambadoro A, Chiani F, Tocchini-Valentini GP: **Three-dimensional microCT imaging of murine embryonic development from immediate post-implantation to organogenesis: application for phenotyping analysis of early embryonic lethality in mutant animals.** *Mamm Genome* 2018, **29**:245-259.
7. Petiet AE, Kaufman MH, Goddeeris MM, Brandenburg J, Elmore SA, Johnson GA: **High-resolution magnetic resonance histology of the embryonic and neonatal mouse: a**

- 4D atlas and morphologic database.** *Proc Natl Acad Sci U S A* 2008, **105**:12331-12336.
8. Zucker RM, Hunter ES, 3rd, Rogers JM: **Apoptosis and morphology in mouse embryos by confocal laser scanning microscopy.** *Methods* 1999, **18**:473-480.
  9. Phoon CK: **Imaging tools for the developmental biologist: ultrasound biomicroscopy of mouse embryonic development.** *Pediatr Res* 2006, **60**:14-21.
  10. Wong MD, van Eede MC, Spring S, Jevtic S, Boughner JC, Lerch JP, Henkelman RM: **4D atlas of the mouse embryo for precise morphological staging.** *Development* 2015, **142**:3583-3591.
  11. Pantazis P, Supatto W: **Advances in whole-embryo imaging: a quantitative transition is underway.** *Nat Rev Mol Cell Biol* 2014, **15**:327-339.
  12. Huang D, Swanson EA, Lin CP, Schuman JS, Stinson WG, Chang W, Hee MR, Flotte T, Gregory K, Puliafito CA: **Optical coherence tomography.** *Science* 1991, **254**:1178-1181.
  13. Syed SH, Larin KV, Dickinson ME, Larina IV: **Optical coherence tomography for high-resolution imaging of mouse development in utero.** *J Biomed Opt* 2011, **16**:046004.
  14. van Velthoven ME, Faber DJ, Verbraak FD, van Leeuwen TG, de Smet MD: **Recent developments in optical coherence tomography for imaging the retina.** *Prog Retin Eye Res* 2007, **26**:57-77.
  15. Tearney GJ, Regar E, Akasaka T, Adriaenssens T, Barlis P, Bezerra HG, Bouma B, Bruining N, Cho JM, Chowdhary S, et al: **Consensus standards for acquisition, measurement, and reporting of intravascular optical coherence tomography studies: a report from the International Working Group for Intravascular Optical Coherence Tomography Standardization and Validation.** *J Am Coll Cardiol* 2012, **59**:1058-1072.
  16. Fan Y, Xia Y, Zhang X, Sun Y, Tang J, Zhang L, Liao H: **Optical coherence tomography for precision brain imaging, neurosurgical guidance and minimally invasive theranostics.** *Biosci Trends* 2018, **12**:12-23.
  17. Raghunathan R, Singh M, Dickinson ME, Larin KV: **Optical coherence tomography for embryonic imaging: a review.** *J Biomed Opt* 2016, **21**:50902.
  18. Larin KV, Larina IV, Liebling M, Dickinson ME: **Live Imaging of Early Developmental Processes in Mammalian Embryos with Optical Coherence Tomography.** *J Innov Opt Health Sci* 2009, **2**:253-259.
  19. Grishina OA, Wang S, Larina IV: **Speckle variance optical coherence tomography of blood flow in the beating mouse embryonic heart.** *J Biophotonics* 2017, **10**:735-743.
  20. Lu GJ, Chou LD, Malounda D, Patel AK, Welsbie DS, Chao DL, Ramalingam T, Shapiro MG: **Genetically Encodable Contrast Agents for Optical Coherence Tomography.** *ACS Nano* 2020, **14**:7823-7831.
  21. Braz AK, de Araujo RE, Ohulchanskyy TY, Shukla S, Bergey EJ, Gomes AS, Prasad PN: **In situ gold nanoparticles formation: contrast agent for dental optical coherence tomography.** *J Biomed Opt* 2012, **17**:066003.
  22. Jia Y, Liu G, Gordon AY, Gao SS, Pechauer AD, Stoddard J, McGill TJ, Jayagopal A, Huang D: **Spectral fractionation detection of gold nanorod contrast agents using optical coherence tomography.** *Opt Express* 2015, **23**:4212-4225.
  23. Jiang X, Tang P, Gao P, Zhang YS, Yi C, Zhou J: **Gold Nanoprobe-Enabled Three-Dimensional Ozone Imaging by Optical Coherence Tomography.** *Anal Chem* 2017, **89**:2561-2568.

24. Kim J, Song X, Ji F, Luo B, Ice NF, Liu Q, Zhang Q, Chen Q: **Polymorphic Assembly from Beveled Gold Triangular Nanoprisms.** *Nano Lett* 2017, **17**:3270-3275.
25. Wi JS, Park J, Kang H, Jung D, Lee SW, Lee TG: **Stacked Gold Nanodisks for Bimodal Photoacoustic and Optical Coherence Imaging.** *ACS Nano* 2017, **11**:6225-6232.
26. Fabris L: **Gold Nanostars in Biology and Medicine: Understanding Physicochemical Properties to Broaden Applicability.** *The Journal of Physical Chemistry C* 2020, **124**.
27. Mousavi SM, Zarei M, Hashemi SA, Ramakrishna S, Chiang WH, Lai CW, Gholami A: **Gold nanostars-diagnosis, bioimaging and biomedical applications.** *Drug Metab Rev* 2020, **52**:299-318.
28. Theodorou IG, Jiang Q, Malms L, Xie X, Coombes RC, Aboagye EO, Porter AE, Ryan MP, Xie F: **Fluorescence enhancement from single gold nanostars: towards ultra-bright emission in the first and second near-infrared biological windows.** *Nanoscale* 2018, **10**:15854-15864.
29. Nguyen VP, Li Y, Henry J, Zhang W, Aaberg M, Jones S, Qian T, Wang X, Paulus YM: **Plasmonic Gold Nanostar-Enhanced Multimodal Photoacoustic Microscopy and Optical Coherence Tomography Molecular Imaging To Evaluate Choroidal Neovascularization.** *ACS Sens* 2020, **5**:3070-3081.
30. Mantri Y, Jokerst JV: **Engineering Plasmonic Nanoparticles for Enhanced Photoacoustic Imaging.** *ACS Nano* 2020, **14**:9408-9422.
31. Yue W, Ali M, Chen K, Ning F, El-Sayed MA: **Gold nanoparticles in biological optical imaging.** *Nano Today* 2019, **24**.
32. Fu Q, Zhu R, Song J, Yang H, Chen X: **Photoacoustic Imaging: Contrast Agents and Their Biomedical Applications.** *Adv Mater* 2019, **31**:e1805875.
33. Attia ABE, Balasundaram G, Moothanchery M, Dinish US, Bi R, Ntziachristos V, Olivo M: **A review of clinical photoacoustic imaging: Current and future trends.** *Photoacoustics* 2019, **16**:100144.
34. Wang LV, Hu S: **Photoacoustic tomography: in vivo imaging from organelles to organs.** *Science* 2012, **335**:1458-1462.
35. Upputuri PK, Pramanik M: **Photoacoustic imaging in the second near-infrared window: a review.** *J Biomed Opt* 2019, **24**:1-20.
36. Zhang Q, Iwakuma N, Sharma P, Moudgil BM, Wu C, McNeill J, Jiang H, Grobmyer SR: **Gold nanoparticles as a contrast agent for in vivo tumor imaging with photoacoustic tomography.** *Nanotechnology* 2009, **20**:395102.
37. Wang J, Xie Y, Wang L, Tang J, Li J, Kocaefe D, Kocaefe Y, Zhang Z, Li Y, Chen C: **In vivo pharmacokinetic features and biodistribution of star and rod shaped gold nanoparticles by multispectral optoacoustic tomography.** *RSC Advances* 2014, **5**:7529-7538.
38. Pan D, Pramanik M, Senpan A, Allen JS, Zhang H, Wickline SA, Wang LV, Lanza GM: **Molecular photoacoustic imaging of angiogenesis with integrin-targeted gold nanobeacons.** *Faseb j* 2011, **25**:875-882.
39. Basak K, Luís Deán-Ben X, Gottschalk S, Reiss M, Razansky D: **Non-invasive determination of murine placental and foetal functional parameters with multispectral optoacoustic tomography.** *Light Sci Appl* 2019, **8**:71.
40. Huang Y, Li M, Huang D, Qiu Q, Lin W, Liu J, Yang W, Yao Y, Yan G, Qu N, et al: **Depth-Resolved Enhanced Spectral-Domain OCT Imaging of Live Mammalian Embryos**

- Using Gold Nanoparticles as Contrast Agent.** *Small* 2019, **15**:e1902346.
41. Ian, Wilmut: **Postimplantation mammalian embryos - a practical approach: edited by A. J. Copp and D. L. Cockroft, IRL Press, 1990. £25.00 (xxi + 357 pages) ISBN 019 963 089 5. Trends in Biotechnology** 1991.
  42. Senthil Kumar P, Pastoriza-Santos I, Rodríguez-González B, Javier García de Abajo F, Liz-Marzán LM: **High-yield synthesis and optical response of gold nanostars.** *Nanotechnology* 2008, **19**:015606.
  43. Keane PA, Ruiz-Garcia H, Sadda SR: **Clinical applications of long-wavelength (1,000-nm) optical coherence tomography.** *Ophthalmic Surg Lasers Imaging* 2011, **42 Suppl**:S67-74.
  44. Adhi M, Liu JJ, Qavi AH, Grulkowski I, Lu CD, Mohler KJ, Ferrara D, Kraus MF, Baumal CR, Witkin AJ, et al: **Choroidal analysis in healthy eyes using swept-source optical coherence tomography compared to spectral domain optical coherence tomography.** *Am J Ophthalmol* 2014, **157**:1272-1281.e1271.
  45. Choma M, Sarunic M, Yang C, Izatt J: **Sensitivity advantage of swept source and Fourier domain optical coherence tomography.** *Opt Express* 2003, **11**:2183-2189.
  46. Vähäkangas K, Myllynen P: **Drug transporters in the human blood-placental barrier.** *Br J Pharmacol* 2009, **158**:665-678.

## Supplementary Files

This is a list of supplementary files associated with this preprint. Click to download.

- [GraphicalAbstract.docx](#)